Journal of Alloys and Compounds 689 (2016) 669–679

Contents lists available at ScienceDirect

Journal of Alloys and Compounds

journal homepage: http://www.elsevier.com/locate/jalcom

Fluorite-pyrochlore phase transition in nanostructured $Ln_2Hf_2O_7$ (Ln = La-Lu)

V.V. Popov [a], A.P. Menushenkov [a, *], A.A. Yaroslavtsev [a, b], Ya.V. Zubavichus [c], B.R. Gaynanov [a], A.A. Yastrebtsev [a], D.S. Leshchev [a], R.V. Chernikov [d]

[a] National Research Nuclear University MEPhI (Moscow Engineering Physics Institute), Moscow, 115409, Russia
[b] European XFEL GmbH, Schenefeld, 22869, Germany
[c] NRC "Kurchatov Institute", Moscow, 123182, Russia
[d] DESY Photon Science, Hamburg, 22607, Germany

ARTICLE INFO

Article history:
Received 23 May 2016
Received in revised form
29 July 2016
Accepted 3 August 2016
Available online 4 August 2016

Keywords:
Lanthanide hafnates
Oxide materials
Precipitation
Pyrochlore
Fluorite
Phase transitions

ABSTRACT

Complex oxides of the $Ln_2Hf_2O_7$ (Ln = lanthanide) series undergo a fluorite to pyrochlore phase transformation. We have studied the whole process of the crystal and local atomic structure realignment during the crystallization and the phase transition in the series of $Ln_2Hf_2O_7$ (Ln = La-Lu) samples synthesized by the coprecipitation method with the subsequent annealing of mixed hydroxides (precursors). The study employed a combination of x-ray diffraction (normal and anomalous), x-ray absorption spectroscopy, analysis of atomic pair distribution function and Raman spectroscopy. The starting and ending temperatures of the fluorite-pyrochlore phase transition for $Ln_2Hf_2O_7$ compounds have been determined along the lanthanide series La-Dy. The scheme summarizing structure types (amorphous, fluorite and pyrochlore) for the whole $Ln_2Hf_2O_7$ (Ln = La-Lu) series as a function of the Ln cation radius (or the $r_{Ln^{3+}}/r_{Hf^{4+}}$ ratio) and the annealing temperature has been refined.

1. Introduction

Complex oxides forming in the Ln_2O_3-MO_2 system (Ln is a lanthanide and M is a titanium subgroup element) have been intensely investigated over recent years because they demonstrate a variety of fascinating physical effects, such as order-disorder phase transitions [1–9], geometrically frustrated magnetism [10], ionic conductivity [11], etc. In addition, these materials have wide technological applications, which include solid electrolytes in high temperature solid oxide fuel cells [11], thermal barrier coatings (TBCs) [12], neutron absorbing [13] and nuclear waste storage materials [14].

The phase diagrams of the Ln_2O_3-MO_2 systems are complicated. They exhibit the formation of several crystal structure types under specific conditions [15]. These include $Ln_2M_2O_7$ complex oxides with pyrochlore-type superstructural ordering of Ln^{3+} and M^{4+} cationic sites and oxygen vacancies (space group $Fd\bar{3}m$) [1–6,15], solid solutions $[LnM]_2O_7$ with disordered fluorite-type cubic (space group $Fm\bar{3}m$) [1–5,15] or monoclinic (space group $P2_1$) structure [6], and rhombohedral δ-phases $Ln_4M_3O_{12}$ (space group $R\bar{3}$) [16]. The formation of a particular structure depends on the synthesis method, the amount of initial oxides Ln_2O_3 and MO_2, and the annealing temperature [1,3–6,17,18]. The formation of a specific phase, sometimes metastable, is essentially controlled by kinetic factors. The concept of kinetic growth-related transition was proposed in Refs. [19–21] to designate such a type of structural rearrangement. The ratio of the cation radii $\gamma = r_{Ln^{3+}}/r_{Hf^{4+}}$ is one of the main factors that determine the resulting crystal structure type [1]. The fluorite-pyrochlore phase transition takes place at a ratio γ~1.46 [1,3–5,18]. According to the recently refined data the limiting ratios for the different $Ln_2M_2O_7$ structure types are as follows: disordered fluorite $\gamma < 1.21 < \delta$-phase $\gamma < 1.42–1.44 <$ pyrochlore $\gamma < 1.78–1.83 <$ monoclinic pyrochlore $\gamma < 1.92$ [22]. The most interesting compounds are located near the lower boundary of the fluorite-pyrochlore solid state phase transition. These compounds show the maximum ionic conductivity [11] and the highest radiation tolerance [23]. The phase transition from an ordered pyrochlore structure to a disordered defect fluorite structure is a rare example of simultaneous disordering in both the cation and anion sublattices. It involves the randomization of the

* Corresponding author.
E-mail address: apmenushenkov@mephi.ru (A.P. Menushenkov).

http://dx.doi.org/10.1016/j.jallcom.2016.08.019
0925-8388/

cations between the 16*c* and 16*d* sites, and the oxygen ions over the 48*f*, 8*b* and 8*a* sites [24,25] (see Fig. 1).

Lanthanide hafnates of the $Ln_2Hf_2O_7$ family remain insufficiently investigated despite the fact that some of these compounds and solid solutions are promising as ceramic layers for TBCs [26] and neutron absorbers [27]. The functionality of these materials depends on the peculiarities of their crystal and local structures. For the lanthanide hafnates the experimentally determined upper boundary of the fluorite-pyrochlore phase transition was put between $Sm_2Hf_2O_7$ and $Eu_2Hf_2O_7$ [28], while the lower boundary lies in the region of $Gd_2Hf_2O_7$ and $Tb_2Hf_2O_7$, which show a cation radii ratio γ close to 1.46 [1,4,5,29]. However, the exact lower boundary position for the phase transition is still under debate. Recent theoretical calculations have demonstrated the trend for pyrochlore ordering in $Dy_2Hf_2O_7$ and $Ho_2Hf_2O_7$ [30,31] and even in $Er_2Hf_2O_7$ [30]. Furthermore, there is experimental evidence of pyrochlore ordering in $Dy_2Hf_2O_7$ obtained from Raman spectroscopy [32].

It should be noted that apart from the chemical composition and geometric factor, the structure of the $Ln_2M_2O_7$ oxides is significantly affected by the crystallite size, which can also be changed by varying the conditions of synthesis [18,33]. When this size is relatively small (1–5 nm), the average crystal structure differs from the local one, although the latter often determines important properties of compounds such as thermal stability, electrophysical and optical properties, catalytic activity, etc. [34].

Apparently, the vast majority of publications are dedicated to the properties of well-crystallized compounds $Ln_2M_2O_7$ [3–6,24,29,35,36] prepared by the solid-state synthesis method at elevated temperature, which does not allow information about changes occurring to the crystal structure during the formation process to be obtained. In this paper we use another synthesis method, based on the annealing of precursors, prepared from the solutions of mixtures of the respective salts [18,37–39].

The synthesis from solutions has the advantage of yielding a highly homogeneous cation distribution within the precursor prepared by the coprecipitation, and allows production of almost single-phase nanocrystalline powders with predetermined composition at lower temperatures [40]. Thus this method is appropriate for studying the evolution of crystalline phases and possible polymorphic transformations during the process of $Ln_2M_2O_7$ synthesis. It can be achieved by annealing the initially amorphous precursors at different temperatures [18].

In recent years we actively investigated the structure formation in boundary compounds: $Gd_2Zr_2O_7$ with $\gamma = 1.46$ [41] and $Ln_2Hf_2O_7$ (Ln = Sm-Dy) with γ = 1.45–1.51 [42–45]. The present work addresses the specific features of lanthanide hafnates $Ln_2Hf_2O_7$ crystal and local structures during their emergence and evolution. The samples have been prepared by annealing initially amorphous precursors at different temperatures in a wider row of lanthanides from La to Lu. In this research we have used the combination of normal and anomalous x-ray diffraction, the local structure sensitive methods of extended x-ray absorption fine structure (EXAFS) and near edge structure (XANES) spectroscopy, the analysis of atomic pair distribution functions (PDF) obtained from the high-energy synchrotron x-ray total scattering, and optical Raman spectroscopy. This combination allowed us to observe the successive realignment of both the cation and anion sublattices during the fluorite-pyrochlore phase transition and to build the scheme summarizing the structure types in the full series of lanthanide hafnates $Ln_2Hf_2O_7$ as a function of the lanthanide type (or Ln^{3+} ion radius) and the annealing temperature.

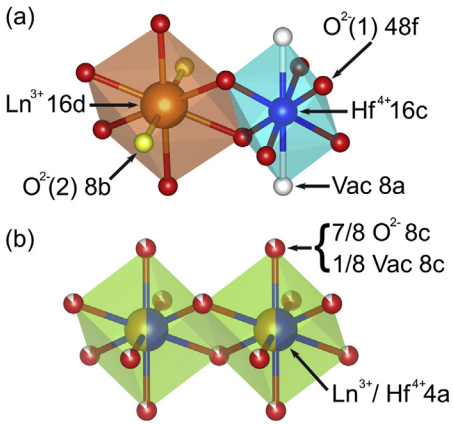

Fig. 1. Representations of the pyrochlore (a) and disordered fluorite structures (b).

2. Experimental

2.1. Synthesis procedure

The lanthanide hafnate series with composition $Ln_2Hf_2O_7$ (Ln = La-Lu) have been synthesized from lanthanide nitrates $Ln(NO_3)_3 \cdot mH_2O$ (the purity 99.96 – 99.99% and m = 4–6 depending on the Ln^{3+} cation) and hafnium oxychloride octahydrate $HfOCl_2 \cdot 8H_2O$ (99.7%) by reverse coprecipitation with subsequent annealing of the resulting mixed hydroxides (precursors). The initial lanthanide and hafnium salts were dissolved while stirring in distilled water. The concentrations of the resulting solutions were determined by inductively coupled plasma atomic emission spectrometry (ICP-AES) using a Vista-PRO (Varian) apparatus. After the determination of concentration of different salt solutions they were mixed in an oxide molar ratio Ln_2O_3:HfO_2 = 1:2. The resulting solution of the salt mixture with a total concentration of 0.5 mol/l was introduced into 3 mol/l aqueous ammonia with vigorous stirring. The resulting suspension of mixed hydroxides (pH 9.5 – 10.0) was filtered and washed with distilled water until the absence of Cl^- anions confirmed by reaction with $AgNO_3$. The resulting wet precipitate was dried to constant weight in a drying cabinet at 90 °C. The dry powders (precursors) were ground in a mortar, heated in a muffle furnace HT 08/18 (Nabertherm) at a rate of 10 K/min to the required temperatures in the range 600–1600 °C, and then annealed isothermally in air for 3 h. The $Dy_2Hf_2O_7$ powder prepared at 800 °C/ 3 h was finely ground in a planetary ball mill (Pulverisette 7 premium line, 1000 rpm, 30 min), pressed uniaxially into cylindrical pellets by applying a pressure of 180 MPa and then sintered in the air in a muffle furnace at a temperature of 1550 °C in Al_2O_3-crucibles for 4 h.

2.2. Sample characterization

Simultaneous thermal analysis (STA) of precursors, involving the measurement of thermogravimetry (TG) and differential scanning calorimetry (DSC) were carried out on a Netzsch STA-409 PC analyzer in the temperature range 30–1400 °C at a heating rate of 10 K/min in an argon flow.

The x-ray powder diffraction of the $Ln_2Hf_2O_7$ series at different temperatures was carried out at the Structural Materials Science beamline of the Kurchatov synchrotron radiation source (Moscow, Russia) [46]. Measurements were performed in the transmission mode at $\lambda = 0.68886$ Å and a sample-detector distance of 200 mm, the beam size 200 × 200 μm, using a 2D detector "Imaging plate Fujifilm BAS-5000". The 2D patterns were integrated and converted to conventional $I(2\theta)$ data using the Fit2D program package [47].

The Rietveld full profile analysis of XRD patterns was performed with the Jana2006 [48]. Crystallographic and the diffraction profile parameters with the coherent scattering lengths (CSL) and microstrains were determined assuming the pyrochlore structure. To enhance the contrast between the Ln^{3+} and Hf^{4+} cations, the diffraction patterns of $Ln_2Hf_2O_7$ samples were additionally measured in resonant (anomalous) diffraction mode at the L_3-Hf absorption edge (9561 eV or $\lambda = 1.29677$ Å).

The total x-ray scattering patterns for the analysis of pair distribution function (PDF) were collected at the P02.1 beamline of the PETRA-III storage ring (DESY Photon Science, Hamburg, Germany) [49] using high-energy photons (59.82 keV, $\lambda = 0.207270$ Å) in transmission mode and a sample-detector distance of 100 mm. The high-energy photons of synchrotron radiation source provide several advantages: high resolution in real space due to the wide range of scattering vector, smaller correction terms (especially for absorption correction), reduction of truncation errors. The 2D scattering curves were recorded using a Perkin Elmer 1621 flat-panel position-sensitive detector. The 2D patterns were integrated and converted to conventional $I(q)$ view using the Fit2D program. The total structure factors and pair distribution functions $G(R)$ were calculated with PDFgetX2 [50]. PDFs for cluster models were simulated using PDFgui [51].

X-ray absorption spectra of $Ln_2Hf_2O_7$ compounds were measured above the L_3-Ln and L_3-Hf absorption edges at the i811 beamline of MAX-Lab (Lund, Sweden) [52] and the mySpot beamline of BESSY-II (Helmholtz-Zentrum Berlin, Germany) [53] in transmission mode at room temperature. The processing and simulation of the EXAFS spectra were performed using VIPER [54] and IFEFFIT [55] program packages. The back scattering amplitudes and phases were calculated with FEFF-8.20 [56] based on the known fluorite and pyrochlore crystal structure parameters and the diffraction data. The XANDA program [54] was used to fit the near-edge region of the x-ray absorption spectra.

The Raman spectra were recorded using a Nicolet iS50 FT-IR spectrometer (Thermo Fisher Scientific Inc.) with Thermo Scientific iS50 Raman module at the Analytical Center of JSC "Scientific Research Institute of Chemical Technology" (Moscow, Russia). The Raman spectra were excited with a laser ($\lambda = 1064$ nm) and measured in the $100 - 3699$ cm^{-1} range. The recorded spectra were averaged over 256 scans with a time interval of 2 s and a resolution of 4 cm^{-1}. The laser focusing points were chosen using an integrated optical microscope, the diameter of the beam focused on the sample was 50 μm.

3. Results and discussion

3.1. Simultaneous thermal analysis

Upon heating the precursor $Ln_2O_3 \cdot HfO_2 \cdot nH_2O$ up to 320 – 350 °C DSC indicates an endothermic process with a minimum at about 130–160 °C regardless the lanthanide type. Meanwhile, the TG curves showed a significant mass loss peak (~60–75% of the total change) due to dehydration, removal of nonstructural water (up to ~200 °C) and further removal of the structured water component in the form of OH groups (>200 °C). Increasing the temperature above 600 °C led to the appearance of a distinct peak in the DSC curve at a constantly decreasing mass of the samples that apparently corresponds to the crystallization process.

An increase in the atomic number along the La-Lu series leads to a decrease in the crystallization temperature from 866 °C (La) to 619 °C (Lu). Also notable is the high degree of hydration of the synthesized precursors $Ln_2O_3 \cdot HfO_2 \cdot nH_2O$ (n~9–11), as well as strong retention of structural OH groups in the forming crystal lattice of complex oxides. This was evidenced by the fact that up to 12–15% of the total mass loss was observed in the temperatures range from 850–1000 ° C (depending on the lanthanide type) to 1400 °C.

3.2. X-ray diffraction analysis

An x-ray diffraction study of the precursors showed that all the synthesized powder samples were x-ray amorphous regardless of the cation type. However, the crystal structure of the precursor particles cannot be considered completely disordered, because one can see several broad peaks at double Bragg angles ~13.5°, ~23.0–23.5° and ~35.0–35.5° (Fig. 2a and b). The crystallite size of ~1 nm was estimated from the width of the most intense peak at 13.5°, although an accurate size determination was complicated by the large width of the peaks.

It was found that crystallization of the $La_2O_3 \cdot HfO_2 \cdot 10.7H_2O$ precursor occurs at 700–800 °C. At 800 °C the powder appears to be nanocrystalline (CSL≈35 nm), and its XRD pattern shows reflections corresponding to the fluorite structure with a unit cell parameter a~5.33 Å. The diffraction pattern for$La_2Hf_2O_7$ starts changing qualitatively at ~1000 °C. The XRD patterns of the powders annealed at ≥1000 °C/ 3 h show the appearance of superstructure peaks (111) (main), (311), (531) and others, which point to the emergence of the pyrochlore-type cation ordering (Fig. 2b). The superstructure reflections appear significantly broader than the basic peaks characteristic of the fluorite structure for the powder $La_2Hf_2O_7$ (1000 °C). The same trend was observed for all oxide systems under study annealed at moderate temperatures (1000–1200 °C). This implies that the cation ordering starts to evolve from separate nanodomains (CSL≈10 nm, as estimated by the Scherrer formula from the widths of most intense pyrochlore superstructure peaks) within the mostly fluorite-type crystallites (CSL≈115 nm from full-profile Rietveld refinement). We have previously observed a similar amorphous-fluorite-pyrochlore phase transformation for $Gd_2Zr_2O_7$ [41].

The investigation has shown that the increase of lanthanide atomic number reduces the crystallization temperature of $Ln_2Hf_2O_7$ powders, which agrees well with the STA data. It was found that at temperature <1000 °C the crystallization of initially amorphous precursor leads to the formation of powders with fluorite structure for all types of the Ln^{3+} ions in $Ln_2Hf_2O_7$ series.

For $Ln_2Hf_2O_7$ (Ln = Pr-Tb) compounds annealed at temperatures ≥1100 °C the XRD patterns also contain peaks which can be ascribed to pyrochlore superstructure reflections. It was observed that the decrease of lanthanide cation radius leads to an increase of the starting temperature of pyrochlore-type ordering and reduces the intensity of superstructure peaks. The annealing temperature increase also resulted in formation of small amount of the HfO_2 impurity (4.1% at 1200 °C and 6.2% at 1400 °C) in $La_2Hf_2O_7$ (Fig. 2b).

In the case of Ln = Dy-Lu similar high-temperature annealing resulted in the preservation of the fluorite structure without any signs of pyrochlore ordering regardless of the Ln type. Besides, unlike in Refs. [16], we have not observed the formation of δ-phases in compounds with the smallest Ln cations (Tm, Yb, Lu), probably because of the rather short annealing time (3 h) and the high rate of sample cooling (~5°/min) after isothermal annealing, which gave rise to the structure quenching.

For the well-crystallized $Ln_2Hf_2O_7$ powders (~1400 °C) we observed a decrease of the lattice parameter a with decreasing Ln^{3+} cation radius for both pyrochlore (Ln = La-Tb) and fluorite (Ln = Dy-Lu) structures. Similar results have been reported in Refs. [4,5].

3.3. Anomalous x-ray diffraction analysis

In non-resonant x-ray diffraction mode, the pyrochlore-type

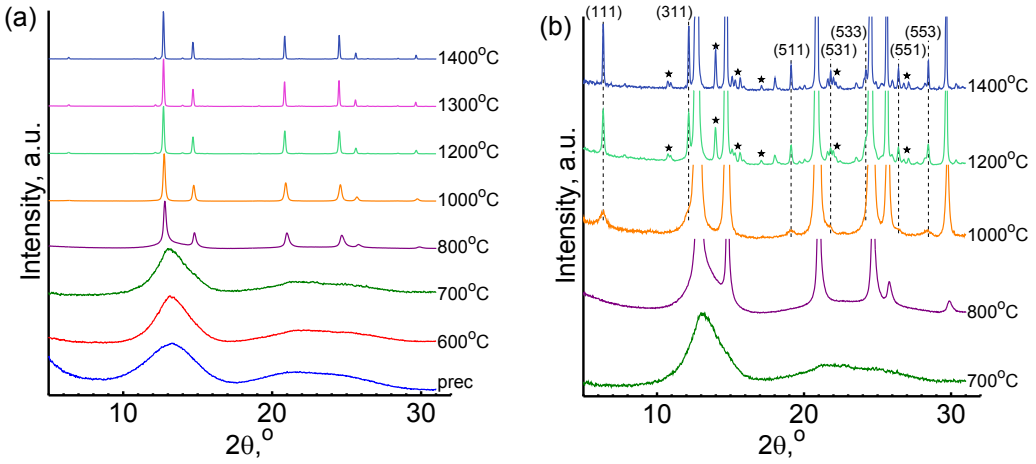

Fig. 2. XRD patterns of $La_2Hf_2O_7$ powders annealed at different temperatures for 3 h in the air: (a) full view; (b) view with the intensity scaled to observe the superstructural peaks. The pyrochlore reflection indexes are marked. * HfO_2 impurity.

superstructure reflections (111), (311), and (511) are extremely weak (less than 1–1.5% of the main peak (222) intensity) (Fig. 2) due to the proximity of atomic numbers of Hf (Z=72) and rare-earth elements from La (Z=57) to Dy (Z=66). In order to enhance the contrast between the lanthanide and hafnium cations we used anomalous (resonant) x-ray diffraction [57,58]. It was found that the experimental intensity of the pyrochlore peaks are significantly altered for photon energies near the L_3-Hf absorption edge (Fig. 3). The effect of anomalous scattering is the most pronounced for the reflection (331), which becomes dominant among the pyrochlore peaks in resonant diffraction mode, whereas it does not exceed the statistical noise in normal diffraction. Such behavior is in good agreement with theoretical simulations for the pyrochlore-type structure. Crystallographic simulations have shown that the resonant intensities of superstructure reflections for the well-crystallized samples $Sm_2Hf_2O_7$, $Eu_2Hf_2O_7$, $Gd_2Hf_2O_7$ annealed at 1400–1500 °C are close to the calculated values or even exceed them. It allowed us to conclude that annealing of these compounds at high temperatures give rise to rather ordered pyrochlore-type structures. However, in the case of $Tb_2Hf_2O_7$ the superstructure peaks are much weaker and wider than those of the defect fluorite ones. Furthermore, for the boundary compound $Dy_2Hf_2O_7$ we did not observe any reflections corresponding to pyrochlore ordering.

Therefore, the results of resonant x-ray diffraction confirm our conclusion that the pyrochlore structure emerges in the form of nanodomains in the well-crystallized fluorite matrix.

3.4. EXAFS data analysis

According to the x-ray diffraction data, we can subdivide all $Ln_2Hf_2O_7$ compounds into two groups depending on the type of crystal structure formed as a result of the high temperature annealing: compounds with Ln = La-Tb, which demonstrate the fluorite-pyrochlore phase transition, and with Ln = Dy-Lu, which retain the fluorite structure. Using EXAFS spectroscopy we have traced the development of the $Ln_2Hf_2O_7$ local atomic structure upon the progressive heat treatment from initially amorphous precursors to well-crystallized powders.

Let us first consider $Ln_2Hf_2O_7$ (Ln = La-Tb) compounds. Fig. 4 shows the Fourier transformation moduli of L_3-Pr and L_3-Hf EXAFS-functions $\chi(k)k^2$ of $Pr_2Hf_2O_7$ powders, annealed at different temperatures.

The first maximum at R~2.0 Å corresponds to the first oxygen coordination shell around praseodymium, or the Pr-O bond. For the sample annealed at 600 °C/ 3 h, which is still amorphous, and for the samples annealed at temperatures <1000 °C/ 3 h with the distinct fluorite structure, the shoulder at ~2.5 Å on the right slope of the main peak is quite small. But with an increase in annealing temperature the oxygen coordination shell starts splitting into two components. This becomes more pronounced at 1200 °C, and for the well-crystallized powder with the pyrochlore structure the second oxygen peak becomes higher than the first one.

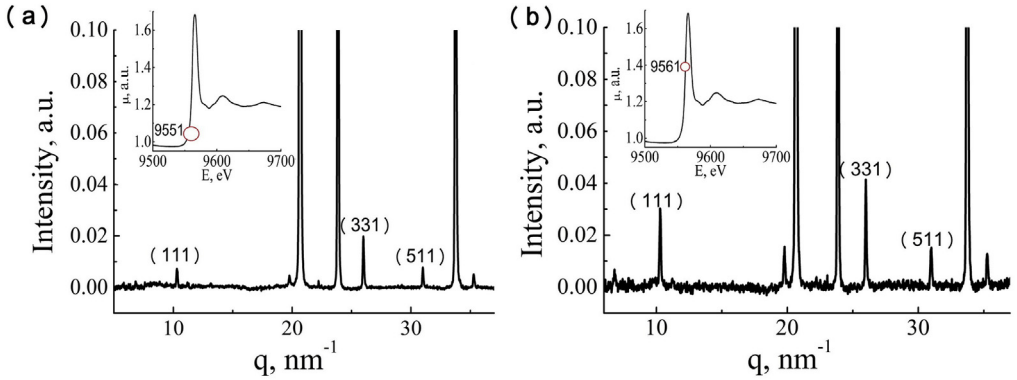

Fig. 3. XRD patterns of $Eu_2Hf_2O_7$ (1600 °C/ 3 h) captured in resonant mode at different photon energies: (a) below the L_3-Hf edge (9551 eV); (b) near the L_3-Hf edge (9561 eV). The pyrochlore reflection indexes are marked. The insets show the L_3-Hf XANES spectra with the diffraction photon energy.

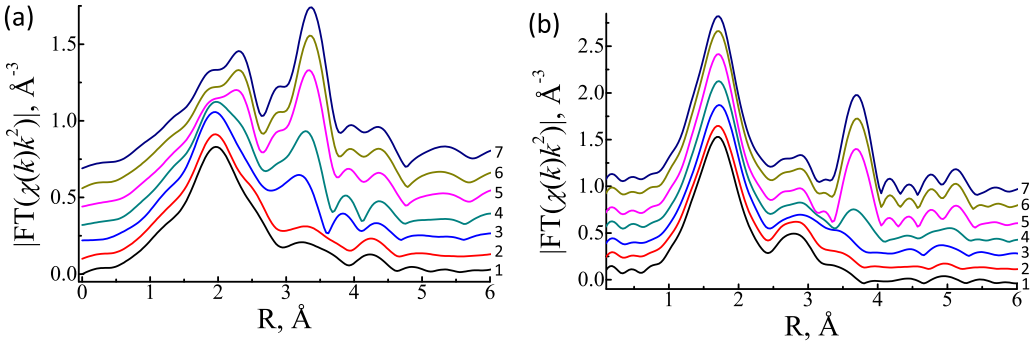

Fig. 4. Fourier transform moduli of EXAFS spectra measured above the L_3-Pr (a) and L_3-Hf edges (b) for $Pr_2Hf_2O_7$ annealed at temperatures: 1 – 600; 2 – 700; 3 – 800; 4 – 1000; 5 – 1200; 6 – 1300; 7 – 1400 °C.

The observed split peak corresponds to two shorter Pr-O(2) and six longer Pr-O(1) distances. The second largest maximum at 3.4 Å includes contributions from Pr-Pr and Pr-Hf interatomic bonds. Its amplitude increases significantly with annealing and the position drifts to larger radius (Fig. 4a). This indicates progressive ordering of the overall crystal structure. At annealing temperature exceeding 1300 °C the peak shape and amplitude substantially stabilize, which corresponds to the end of the pyrochlore structure formation.

Similarly, two distinct peaks corresponding to the bonds Hf-O (1.7 Å) and Hf-(Hf,Pr) (3.7 Å) are observed at the L_3-Hf edge (Fig. 4b). Unlike the L_3-Pr case, the annealing temperature increase does not lead to splitting of the Hf-O shell into two components, since the pyrochlore structure is characterized by only one Hf-O bondlength. Besides, the Hf-(Hf,Pr) maximum still remains smaller than the Hf-O peak, which possibly indicates a more disordered nature of the Hf^{4+} ions distribution in the lattice than of the lanthanides.

Results of L_3-Hf and L_3-Pr EXAFS-spectra simulation for the series of different annealing temperatures are shown in Fig. 5. Indeed, the annealing temperature increase leads to a remarkable splitting of the Pr-O coordination shell into two components upon the fluorite-pyrochlore transition. At the same time, the Pr-O(1) and Pr-Hf interatomic distances increase, while the Pr-O(2), Hf-O, Pr-Pr and Hf-Hf distances decrease. The Debye-Waller factors for all bonds also decrease with progressive annealing, indicating the ordering process in the investigated powders.

Similar behavior of the local structure including the splitting of the first Ln-O oxygen shell has been observed in other $Ln_2Hf_2O_7$ (Ln = La, Nd, Sm, Eu) compounds, characterized by the amorphous-fluorite-pyrochlore phase transitions.

For $Dy_2Hf_2O_7$, which has the fluorite structure according to diffraction data, we did not observe splitting of the Dy-O peak, unlike in $Pr_2Hf_2O_7$ (Fig. 6a). The Dy-O and Hf-O bond lengths decrease slightly with the annealing temperature increasing up to 1000 °C, while Dy-Hf and Dy-Dy, Hf-Hf interatomic distances slightly increase or rather stay virtually constant (Fig. 6b). When the annealing temperature exceeds 1000–1200 °C, all the local structure parameters (bond lengths, Debye-Waller factors, coordination numbers) remain almost unchanged, indicating that the formation of the fluorite structure in the samples is essentially complete.

Notably, all the investigated $Ln_2Hf_2O_7$ samples with the fluorite structure are characterized by a pronounced nonequivalence of the local environment of the Ln^{3+} and Hf^{4+} cations due to the observed difference in the Ln-O and Hf-O bond lengths (Figs. 4–6), which significantly exceeds the standard error of the interatomic distances determination by EXAFS (0.01–0.02 Å). For an ideal fluorite structure, both the Ln-O and M-O distances should be equal to $\sqrt{3}/4 \times a$, where a is the cubic cell parameter, i.e. ~2.26 and 2.33 Å for $Tb_2Hf_2O_7$ and $La_2Hf_2O_7$, respectively, since Ln and M atoms occupy formally the same crystallographic site. This means that the local environment of two types of cations in fluorite $Ln_2Hf_2O_7$ powders cannot be described by the ideal fluorite model, and is rather characterized by the defect-fluorite structure with nonequivalent positions of Ln^{3+} and Hf^{4+} cations. This assumption is confirmed by calculations which showed that the Dy-O and Hf-O coordination numbers in $Dy_2Hf_2O_7$ are close to 7 over the entire annealing temperature range (up to 1400 °C) [43]. This indicates the possible presence of oxygen vacancies, typical for the formation of a defect-fluorite structure (anion-deficient fluorite-related structure).

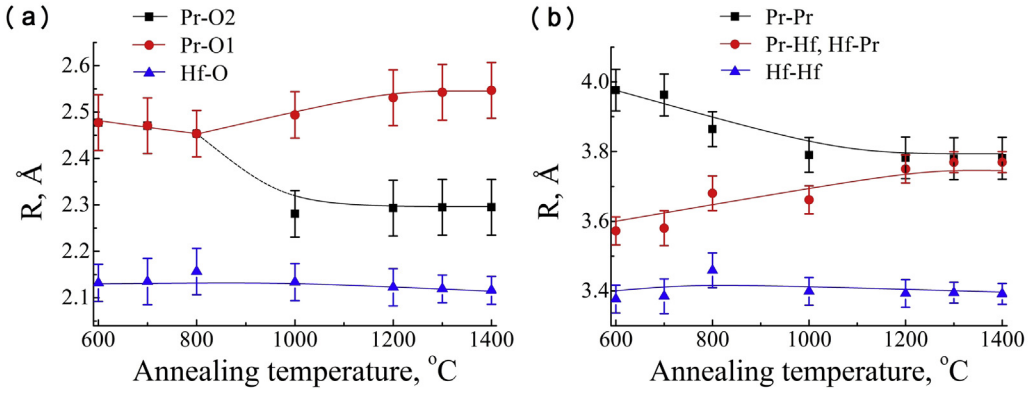

Fig. 5. Bond lengths obtained from EXAFS simulation vs. annealing temperature for Pr-O and Hf-O bonds (a) and Pr-Pr, Hf-Hf and Pr-Hf bonds (b) in $Pr_2Hf_2O_7$ series.

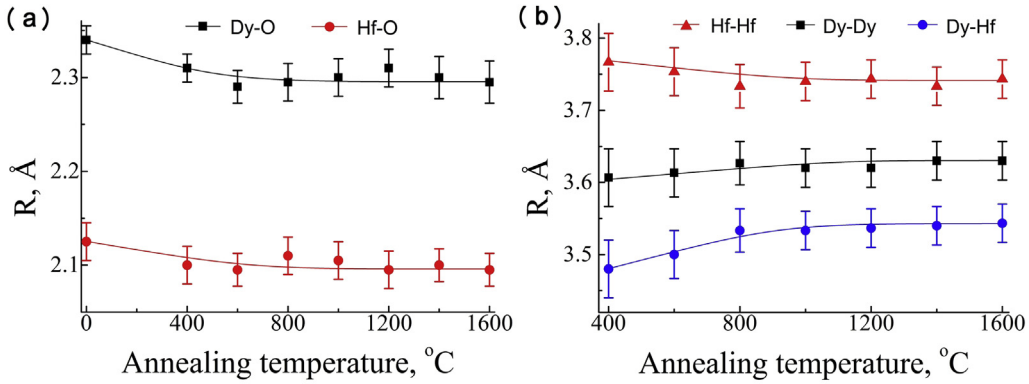

Fig. 6. Bond lengths obtained from EXAFS simulation vs. annealing temperature for Dy-O and Hf-O bonds (a) and Dy-Dy, Hf-Hf and Dy-Hf bonds (b) in $Dy_2Hf_2O_7$ series.

3.5. XANES data analysis

Additional information about changes in the local environment of cations in $Ln_2Hf_2O_7$ powders occurring during the heat treatment of amorphous precursor was obtained from the analysis of XANES-spectra.

It was found that for pyrochlore compounds $Ln_2Hf_2O_7$ (Ln = La-Tb) an increase in the annealing temperature up to 1000 °C, which induces the transition from amorphous (precursor) to the nanocrystalline fluorite structure, leads to broadening of L_3-Hf XANES region (Fig. 7a). A further temperature rise (up to 1000–1200 °C depending on the type of the Ln^{3+} cation) leading to the appearance of pyrochlore structure is accompanied not only by a further increase of the width of absorption maximum, but also by its splitting in two components (Fig. 7b), which indicates a change in the symmetry of local Hf environment. This agrees well with the data given in Refs. [5], since the coordination number of M^{4+} cations changes from 8 to 6 upon the fluorite-pyrochlore phase transition. For L_3-Ln edge we observe only broadening of the absorption maximum without splitting over the entire annealing temperature range.

However, in the case of $Tb_2Hf_2O_7$ it was found that the L_3-Tb XANES spectrum contained two contributions, which corresponds rather to Tb^{3+} and Tb^{4+} oxidation states. The highest Tb^{4+} content of ~7–8% was estimated for the $Tb_2Hf_2O_7$ sample annealed at 1000 °C.

3.6. PDF analysis

The assumption made from the results of EXAFS spectroscopy concerning the evolution of local atomic structure of $Ln_2Hf_2O_7$ with progressive annealing were confirmed by another local structure sensitive method, the analysis of the atomic pair distribution function. The total x-ray scattering patterns for PDF analysis were measured in high-q mode using high-energy photons from a synchrotron radiation source in order to enhance the real-space resolution.

The pair distribution functions $G(R)$ for $Gd_2Hf_2O_7$ powders annealed at different temperatures in the range of the fluorite-pyrochlore phase transition are shown in Fig. 8. With an increase in annealing temperature, we observe the progressive emergence of distinct narrow maxima in the $G(R)$ function corresponding to the individual coordination shells in the local environment of atoms. The increase of structural order appears here as an expansion of the real space range, in which the pair correlation maxima are still distinguishable. This distance is also related to the crystallite size due to the rapid decay of the PDF function outside the crystallites because of their random orientation relative to each other. And although it is also limited by the angular resolution of the instrument in reciprocal space, for the samples annealed at low temperature (≤800 °C) the crystallite sizes obtained from the analysis of PDF data still qualitatively correlate with CSL dimensions defined from the XRD peak broadening. Values of the lattice parameter a, determined from the fitting of high-q diffraction patterns, are also in a good agreement with those previously determined from powder diffraction.

The behavior of $G(R)$ at relatively small R is shown in Fig. 8b. The local structure of samples varies strongly with increasing annealing temperature: the distinct peaks corresponding to individual coordination shells in the local environment of atoms form gradually. The first two peaks of the pair distribution

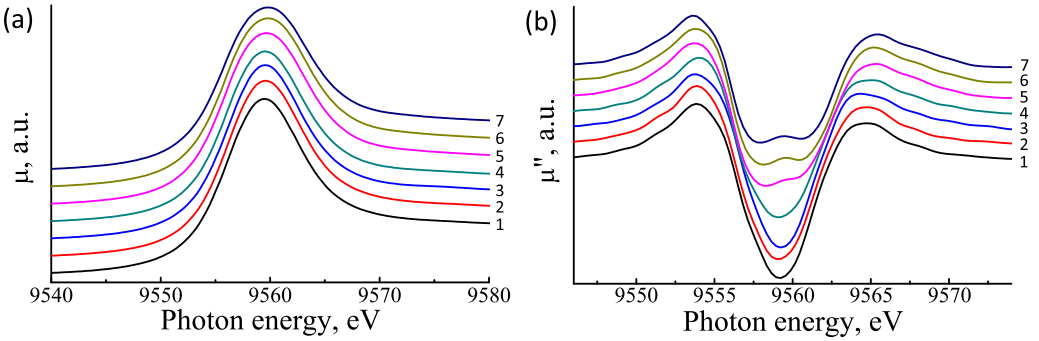

Fig. 7. XANES spectra (a) and their second derivatives (b) for $Pr_2Hf_2O_7$ annealed at temperatures: 1 – 600; 2 – 700; 3 – 800; 4 – 1000; 5 – 1200; 6 – 1300; 7 – 1400 °C. The second derivative plot clearly shows the splitting of absorption maximum.

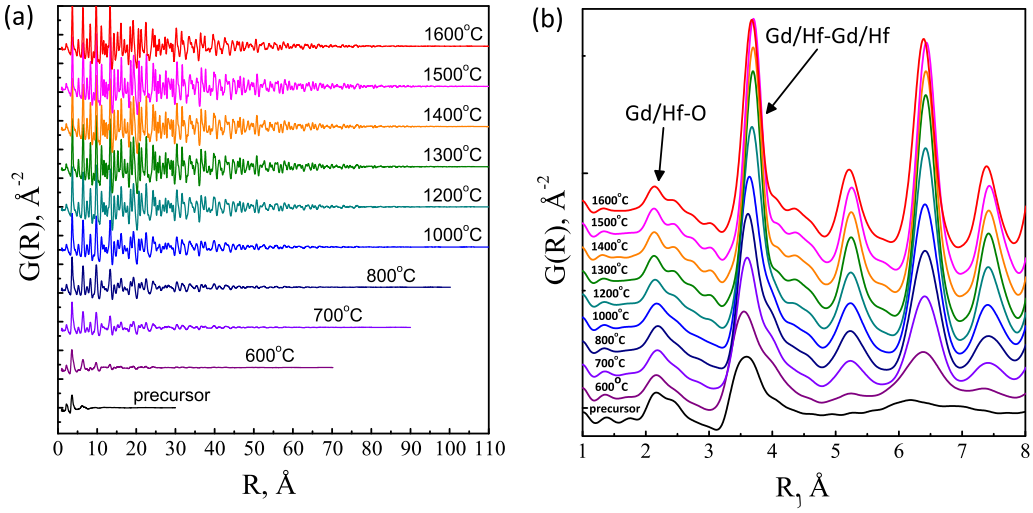

Fig. 8. Full (a) and detailed (b) view of pair distribution functions $G(R)$ for $Gd_2Hf_2O_7$ annealed at different temperatures.

function corresponding to the interatomic distances Gd/Hf-O and Gd/Hf-Gd/Hf have an asymmetric shape that is consistent with the EXAFS data regarding the nonequivalence of the local environment of Gd^{3+} and Hf^{4+} cations in all samples of this series. An amorphous precursor peak corresponding to the metal-oxygen bond Gd/Hf-O has the most symmetrical and integral shape, which can be explained by the diversity of metal-oxygen interatomic distances in the absence of crystalline ordering. During the initial stages of crystallization the peak shape varies considerably: there is a pronounced asymmetry, indicating that a few typical bonds with certain lengths are forming. With further increase of the annealing temperature, accompanied by the growth of pyrochlore domains, the peak asymmetry is enhanced, which correlates with a splitting of the Gd-O bond lengths as established by EXAFS. The second maximum of the $G(R)$ function corresponding to the bunch of metal-to-metal (Gd/Hf-Gd/Hf) distances (Fig. 8b) is less asymmetrical compared to the first oxygen peak. However, the observed changes of the peak width still point to the existence of a systematic variation of respective distances.

While the maxima of $G(R)$ corresponding to the Gd/Hf-O bonds are in good agreement with the coordination shell radii obtained from EXAFS, the correspondence is worse for the metal-metal correlations (Fig. 9a). This can be explained assuming that the model used for simulation of metal-metal shell contribution to the EXAFS-function does not perfectly represent the real structure of the compounds. We speculate that the pyrochlore phase is by far not perfect due to the presence of antisite defects $Gd_{Hf} + Hf_{Gd}$ (i.e., gadolinium in hafnium sites and vice versa). As a result, there might be some local distortions in the positions of Gd and Hf atoms, so that the scatter in Gd/Hf-Gd/Hf distances is even larger.

The local region of pair distribution functions $G(R)$ for the fluorite $Dy_2Hf_2O_7$ samples reveals the asymmetrical shape of the Dy/Hf-O and Dy/Hf-Dy/Hf peaks as well, indicating the difference between the local environment of Dy^{3+} and Hf^{4+} cations. The shape and intensity of the first peak corresponding to Dy/Hf-O bonds is almost unchanged, suggesting that the Hf-O and Dy-O bond lengths do not change much with annealing, which agrees quite well with the EXAFS results (Fig. 6a). The Dy-Dy bond lengths for well-crystallized samples (annealing temperature $\geq$1200 °C) are also in a good agreement with the coordination shell radii obtained from EXAFS (Fig. 9b). The similarity of the PDF and EXAFS results in $Dy_2Hf_2O_7$ for both the oxygen and metal shells suggests that although this compound forms a disordered fluorite structure, on average it is probably more homogeneous than the structure of pyrochlore phases with lighter Ln^{3+} cations.

PDF functions for $Dy_2Hf_2O_7$ samples were simulated based on the fluorite structure model. It was found that the fluorite model describes the long-range order of the crystal structure well, but fails to describe the local range at R<8 Å, because it does not take into account the different local environments of the Dy^{3+} and Hf^{4+} cations. This confirms the formation of a defect-fluorite structure in $Dy_2Hf_2O_7$.

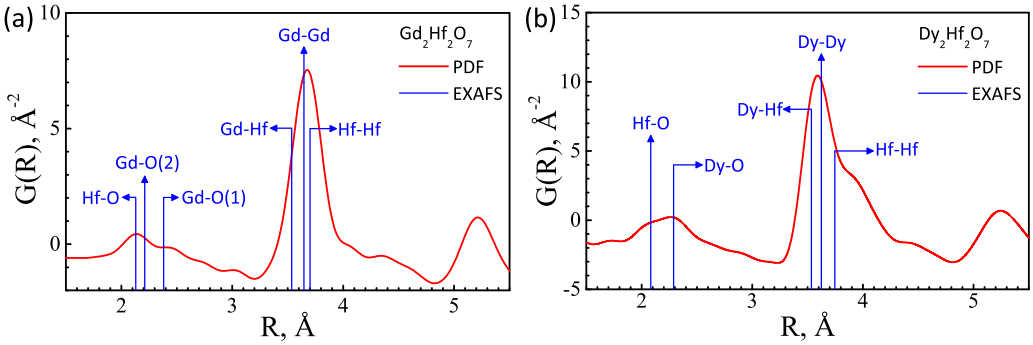

Fig. 9. Comparison of interatomic distances obtained from EXAFS analysis (marked with vertical lines) with the positions of the corresponding components of the PDF $G(R)$ (red curve) for the $Gd_2Hf_2O_7$ (a) and $Dy_2Hf_2O_7$ (b) powders synthesized at 1600 °C.

3.7. Raman spectroscopy

Raman spectroscopy is sensitive mostly to oxygen-cation vibrations. In the cubic pyrochlore structure the lanthanide cations and hafnium cations located at sites 16*d* and 16*c*, respectively, do not contribute to the Raman spectrum since they occupy centrally symmetric positions (Fig. 1). Therefore, the observed six Raman bands are associated exclusively with the oxygen positions O(1) and O(2). The Raman-active modes per set of oxygen anions in the case of the pyrochlore structure are as follows:

$O(1)_{48f}$ anion: $A_{1g} + E_g + 3F_{2g}$

$O(2)_{8b}$ anion: F_{2g}

In the case of the fluorite structure, the Raman spectrum contains only a triply degenerate F_{2g} mode associated with the O(2) position.

At annealing temperatures <900 °C we observed no distinct pyrochlore modes in the Raman spectra of any of the studied $Ln_2Hf_2O_7$. Increasing the annealing temperature to ≥1000 °C leads to the emergence of these modes. Analysis of the $La_2Hf_2O_7$ Raman spectra (Fig. 10a and b) showed that the formation of crystal structure with the pyrochlore-type anion sublattice occurs at 1000 °C. All six pyrochlore modes E_g (321 cm^{-1}), A_{1g} (499 cm^{-1}) and $4F_{2g}$ (304 main, 401, 520 and 755 cm^{-1}) are well resolved in the Raman spectra of $La_2Hf_2O_7$ prepared at temperatures ≥1000 °C. These results are in good agreement with the experimental and calculated data reported in Ref. [59]. The detailed analysis of the spectra of $La_2Hf_2O_7$ annealed at temperatures ≥1200 °C showed the weak modes characteristic of monoclinic HfO_2 (134, 147 cm^{-1}). The amount of HfO_2 impurity was estimated as 4.4% at 1200 °C and 6.1% at 1400 °C, which is in good agreement with the XRD results.

The effect of the rare-earth ion type on the Raman spectra of well-crystallized powder $Ln_2Hf_2O_7$ (Ln = La-Dy) is shown in Fig. 11a. From La to Dy the Raman peaks become wider and shift to higher wave numbers. Thus the most intense F_{2g} mode (~305 cm^{-1}) in the Raman spectra of $Dy_2Hf_2O_7$ is approximately one order of magnitude broader than that of $La_2Hf_2O_7$. This agrees well with the results of [5].

The combined analysis of Raman and XRD data shows that the fluorite-pyrochlore phase transition is accompanied by a reduction in the width of the observed maxima corresponding to the pyrochlore Raman modes (Fig. 10a). Therefore, the Raman peak width (FWHM) can be used as a quantitative criterion in the analysis of pyrochlore anionic sublattice ordering by analogy with cation sublattice ordering from x-ray diffraction data (Fig. 2). In this analysis the FWHM of the most intense Raman peak (~300–305 cm^{-1}) was used.

In Fig. 11b it is shown that a sharp decrease in FWHM for $La_2Hf_2O_7$ starts at 900 °C, which probably indicates the onset of the pyrochlore anion ordering in the crystal structure. At the same time, according to the XRD data (Fig. 2b) the pyrochlore cationic ordering in $La_2Hf_2O_7$ becomes evident only at 1000 °C. Increasing the annealing temperature above 1100 °C barely affects the FWHM, probably indicating the completion of the pyrochlore anionic sublattice formation in $La_2Hf_2O_7$. Consequently, the inflection point in the temperature dependence of the FWHM (at 1030 °C) in the Raman data can be assigned to the completion temperature of the pyrochlore structure formation. Notably, the starting and the ending temperatures of pyrochlore ordering obtained from Raman studies are in a good agreement with EXAFS results.

As it was shown in Refs. [60], a similar structural rearrangement in pyrochlore titanates $RE_2Ti_2O_7$ (RE = Y, Gd and Dy) from a totally disordered to a more ordered state includes two competing processes, a diffusionless ordering within the oxygen anion sublattice and the rearrangement of cation sublattice. Thus we suppose that these two types of ordering processes are common for all systems with the fluorite-pyrochlore transition.

The starting and the ending temperatures of pyrochlore ordering in the anionic sublattice strongly depend on the type of cation in $Ln_2Hf_2O_7$ (Fig. 11b). The FWHM inflection point moves from ~1030 °C for $La_2Hf_2O_7$ to 1500 °C for $Gd_2Hf_2O_7$. It suggests that the increase of the lanthanide atomic number accompanied by a decrease of the Ln^{3+} cation radius and the ratio $\gamma = r_{Ln^{3+}}/r_{Hf^{4+}}$ leads to additional disordering in the pyrochlore anionic sublattice in $Ln_2Hf_2O_7$, resulting in the preservation of fluorite structure, in good agreement with the XRD data.

Interestingly, for $Gd_2Hf_2O_7$ with a further increase in the annealing temperature up to 1600 °C the Raman peak FWHM starts increasing again. This is probably explained either by the appearance of the HfO_2 phase impurities observed in XRD patterns and Raman spectra, or by the onset of the inverse solid-phase transition from pyrochlore to fluorite structure.

The Raman spectrum of a $Dy_2Hf_2O_7$ ceramic pellet synthesized at 1550 °C/ 4 h contains a doublet with a broad maximum at ~320, 410 cm^{-1} and a weaker contribution at 620 cm^{-1} (Fig. 11a) in a good agreement with [5,32], clearly demonstrating the tendency towards pyrochlore-type anionic ordering in $Dy_2Hf_2O_7$. The apparent discrepancy between the results of Raman spectroscopy and XRD data for $Dy_2Hf_2O_7$ is probably due to the imperfect structure of the samples, which is characterized by numerous antisite defects [61]. This prevents the pyrochlore-type cationic ordering and strongly suppresses the superlattice peaks in XRD.

Thus, the comparison of all available experimental data shows

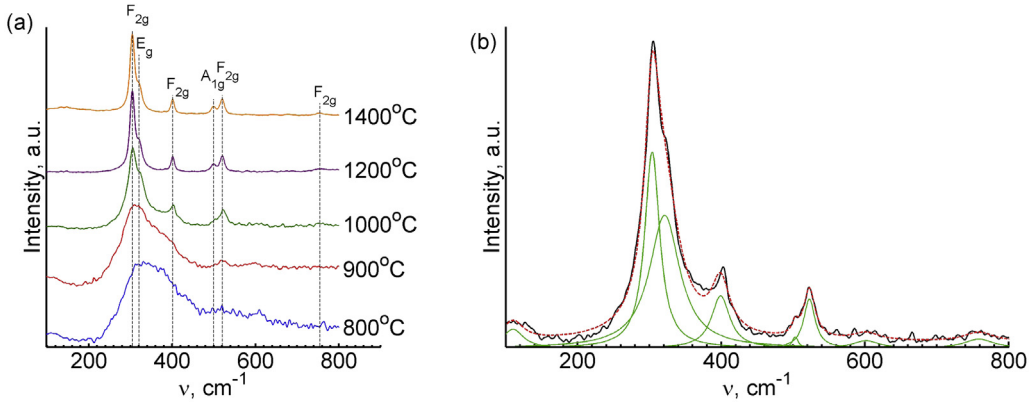

Fig. 10. Raman spectra of $La_2Hf_2O_7$ annealed at different temperatures (a). Raman spectrum of $La_2Hf_2O_7$ (1000 °C): solid black – experimental spectrum; solid green – Lorentz fitting curves; dashed red – summary fitting curve (b).

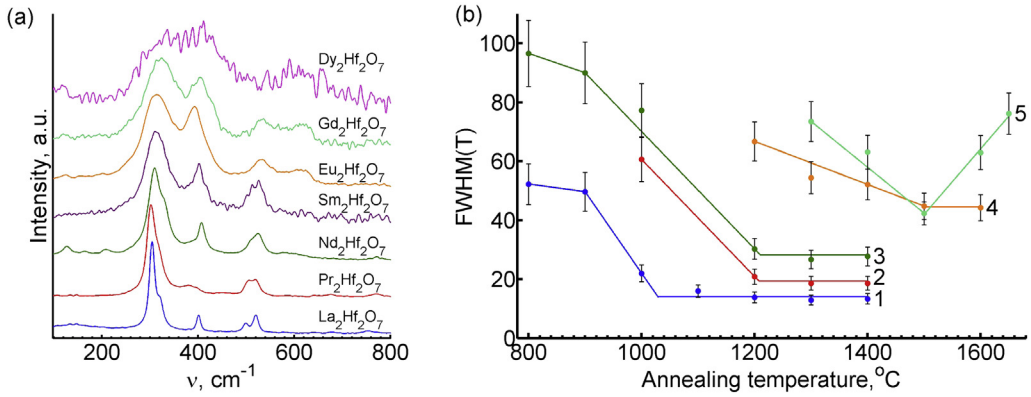

Fig. 11. Raman spectra of $Ln_2Hf_2O_7$ (Ln = La-Tb) powders annealed at 1400 °C and a $Dy_2Hf_2O_7$ ceramic pellet annealed at 1550 °C (a). FWHM of Raman mode 300–305 cm^{-1} vs. annealing temperatures for different $Ln_2Hf_2O_7$ powders: 1 – $La_2Hf_2O_7$; 2 – $Pr_2Hf_2O_7$; 3 – $Nd_2Hf_2O_7$; 4 – $Eu_2Hf_2O_7$; 5 – $Gd_2Hf_2O_7$ (b).

that Raman spectroscopy is indeed a highly efficient technique to probe the local structure evolution in the anionic sublattice of complex oxides $Ln_2Hf_2O_7$.

3.8. Scheme of structure types in $Ln_2Hf_2O_7$

The results of our comprehensive study of the crystal and local structure peculiarities in the $Ln_2Hf_2O_7$ series are summarized in Fig. 12 as a scheme depicting specific stability ranges of different crystal structure types (i.e. amorphous, fluorite and pyrochlore) vs. the Ln^{3+} radius and the synthesis temperature, taking into account also the available literature data. It should be noted that some structural transformations shown in the scheme are kinetically controlled and thus the respective temperatures can be dependent to some extent on the details of synthesis procedure, such as the duration of high temperature treatment or the quenching rate.

The initial crystallization of amorphous precursors leads to the formation of nanocrystalline oxides with the fluorite structure regardless the Ln^{3+} cation type. The crystallization onset temperature is lower for $Ln_2Hf_2O_7$ with heavier Ln or, equivalently, with a smaller Ln^{3+} cation radius and $\gamma = r_{Ln^{3+}}/r_{Hf^{4+}}$ ratio (curve 1 in Fig. 12, according to DSC data). In contrast, the fluorite-pyrochlore phase transition temperature becomes higher along the same series (curve 2 in Fig. 12, based on XRD data). It is shown that the transition from the fluorite to pyrochlore structure happens in a gradual way and includes a stage of formation of pyrochlore-type nanodomains in the well-crystallized fluorite matrix and thus can be classified as a kinetic (growth-related) transition according to [19–21].

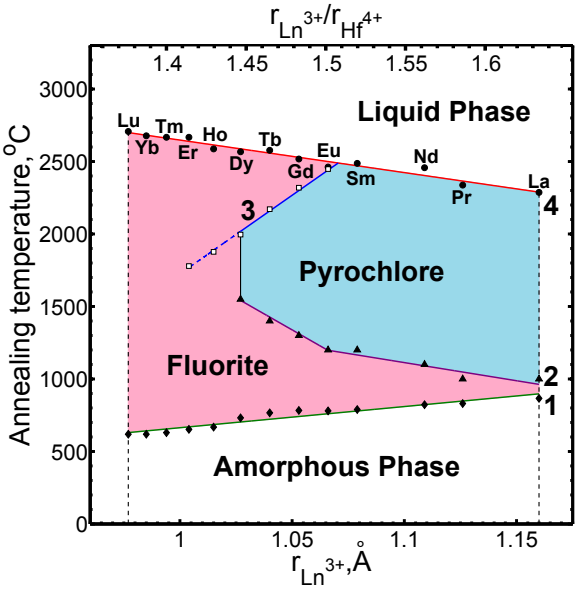

Fig. 12. Scheme of structure types in $Ln_2Hf_2O_7$ compounds obtained by annealing of amorphous precursors prepared by coprecipitation from salt solution vs. the Ln^{3+} radius (or the $r_{Ln^{3+}}/r_{Hf^{4+}}$ ratio) and annealing temperature. 1 – crystallization temperature from DSC; 2 – fluorite-pyrochlore transition temperature from XRD for $La_2Hf_2O_7$ – $Tb_2Hf_2O_7$ and Raman results for $Dy_2Hf_2O_7$; 3 – pyrochlore-fluorite transition temperature from Refs. [30]; 4 – melting temperature from Ref. [15].

Polycrystalline oxides annealed at higher temperatures are characterized by local structure ordering both in the anion and cation sublattices, as evidenced by Raman and EXAFS data, which additionally allowed us to identify the onset and completion temperatures of the phase transition. EXAFS data reveal splitting of the Ln-O bond into two components for all pyrochlore compounds.

A further increase of the annealing temperature leads to congruent melting of $La_2Hf_2O_7$ and $Pr_2Hf_2O_7$ (i.e. the liquid has the same composition as the compound), incongruent melting of $Nd_2Hf_2O_7$ and $Sm_2Hf_2O_7$ [62], and a reversible solid state pyrochlore-fluorite (order-disorder) phase transition experimentally observed in $Ln_2Hf_2O_7$ (Ln = Eu-Tb) [1,4,5,29] and theoretically predicted in $Ln_2Hf_2O_7$ (Ln = Dy-Er) [30,31,62]. The experimental and theoretical values of the pyrochlore-fluorite transition temperature differ considerably [25]. Common to all works is that the phase transition temperature decreases with the radius of the Ln^{3+} cation (curve 3 in Fig. 12, based on the results of [30]), while the melting point rather increases through the $Ln_2Hf_2O_7$ series (curve 4 in Fig. 12, based on the results of [15]).

It is noteworthy that the position of an inflection in curve 2 near $Eu_2Hf_2O_7$ corresponds well to the data in Ref. [28] for the upper boundary of the solid phase pyrochlore-fluorite transition. Moreover, it was found that the lower boundary of pyrochlore phase stability occurs at $Dy_2Hf_2O_7$.

We found no trace of the pyrochlore structure in $Ln_2Hf_2O_7$ (Ln = Ho, Er), predicted theoretically in Refs. [30,31]. Besides, no δ-phase formation was observed for $Ln_2Hf_2O_7$ (Ln = Tm, Yb, Lu) (Fig. 12), in contrast to other reports [16].

4. Conclusion

Comprehensive studies of $Ln_2Hf_2O_7$ (Ln = La-Lu) oxides, synthesized by coprecipitation with subsequent annealing of the precursors, using a combination of x-ray, synchrotron and optical

methods has shown that regardless the type of lanthanide cation, the initial crystallization of amorphous precursors results in the formation of nanocrystalline powders with the fluorite structure. The crystallization is facilitated for heavier lanthanides with smaller cationic radii. At higher temperatures, the fluorite-pyrochlore phase transition occurs for Ln = La-Dy. The boundary compound $Dy_2Hf_2O_7$ shows traces of pyrochlore ordering in the Raman data, although does not show any signs of superstructure in x-ray diffraction. Characteristic temperatures for the ordering in the cationic and anionic sublattices are slightly different (lower for the anionic sublattice) but both increase for the light lanthanides with decreasing Ln^{3+} cation radius (or the $r_{Ln^{3+}}/r_{Hf^{4+}}$ ratio). It was shown that the transition from the fluorite to pyrochlore structures for Ln = La-Dy proceeds via the intermediate emergence and progressive growth of pyrochlore-type nanodomains in a fluorite matrix. In the case of compounds with smaller Ln^{3+} cationic radii (Ln = Tm, Yb, Lu) no formation of the δ-phases was observed. The fluorite-pyrochlore phase transition has distinct manifestation in all experimental techniques we applied. In particular, the splitting of the first coordination shell Ln-O into two components is a pyrochlore structure marker from the EXAFS viewpoint. In XRD, the pyrochlore phase appears in a set of relatively weak superstructure reflections that are hugely enhanced in anomalous diffraction mode near the L_3-Hf edge. In compounds which retain the fluorite structure upon annealing (i.e. $Dy_2Hf_2O_7$) considerable nonequivalence of the cation local environment was observed. Based on the complementary experimental data obtained we have refined the scheme of structural transformations in the $Ln_2Hf_2O_7$ (Ln = La-Lu) systems by identifying stability regions of different structural types and essential boundary conditions.

Acknowledgements

The authors acknowledge DESY Photon Science (Hamburg), Helmholtz-Zentrum Berlin, MAX IV (Lund), Kurchatov synchrotron center (Moscow) and JSC “Scientific Research Institute of Chemical Technology” (Moscow) for providing the opportunity of XAFS, XRD, PDF and Raman spectroscopy measurements and Dr. J. Bednarcik, Dr. N. Tsarenko, Dr. I. Zizak, Dr. D. Wallacher, Dr. R. Carley and E. Kulik for the help in experiments, data analysis and manuscript preparation. This work was financially supported by the Russian Science Foundation in according with Grant 14-22-00098.

References

[1] M. Subramanian, G. Aravamudan, G. Subba Rao, Oxide pyrochlores – a review, Prog. Solid State Chem. 15 (1983) 55–143.
[2] J. Shamblin, M. Feygenson, J. Neuefeind, C. Tracy, F. Zhang, S. Finkeldei, D. Bosbach, H. Zhou, R. Ewing, M. Lang, Probing disorder in isometric pyrochlore and related complex oxides, Nat. Mater. 15 (2016) 507–511.
[3] P. Blanchard, R. Clements, B. Kennedy, C. Ling, E. Reynolds, M. Avdeev, A. Stampfl, Z. Zhang, L.-Y. Jang, Does local disorder occur in the pyrochlore zirconates? Inorg. Chem. 51 (2012) 13237–13244.
[4] C. Karthik, T. Anderson, D. Gout, R. Ubic, Transmission electron microscopic study of pyrochlore to defect-fluorite transition in rare-earth pyrohafnates, J. Solid State Chem. 194 (2012) 168–172.
[5] P. Blanchard, S. Liu, B. Kennedy, C. Ling, M. Avdeev, J. Aitken, B. Cowie, A. Tadich, Investigating the local structure of lanthanoid hafnates $Ln_2Hf_2O_7$ via diffraction and spectroscopy, J. Phys. Chem. C 117 (2013) 2266–2273.
[6] J. Farmer, L. Boatner, B. Chakoumakos, M.-H. Du, M. Lance, C. Rawn, J. Bryan, Structural and crystal chemical properties of rare-earth titanate pyrochlores, J. Alloys Compd. 605 (2014) 63–70.
[7] L. Fomina, S. Pal'guev, The mechanism of formation of $Sm_2Zr_2O_7$ and $Gd_2Zr_2O_7$ with the pyrochlore structure, Zh. Neorg. Khim. (Russ.) 22 (1977) 326–330.
[8] V. Glushkova, Phase Transitions in Mixed Oxides of Zirconium, Hafnium and Rare-earth Elements, Dr. Sci. Chem. thesis, ISC Akad. Nauk SSSR, Leningrad, 1972.
[9] E. Isupova, V. Glushkova, E. Keler, A study of the Gd_2O_3-HfO_2 system in the composition range enriched with hafnia, Izv. Akad. Nauk. SSSR, Neorg. Mater. (Russ.) 4 (1968) 1732–1737.
[10] J. Gardner, M. Gingras, J. Greedan, Magnetic pyrochlore oxides, Rev. Mod. Phys. 82 (2010) 53–107.
[11] H. Yamamura, H. Nishino, K. Kakinuma, K. Nomura, Electrical conductivity anomaly around fluorite-pyrochlore phase boundary, Solid State Ionics 158 (2003) 359–365.
[12] W. Pan, S. Phillpot, C. Wan, A. Chernatynskiy, Z. Qu, Low thermal conductivity oxides, MRS Bull. 32 (2012) 917–922.
[13] V. Risovany, A. Zakharov, E. Muraleva, V. Kosenkov, R. Latypov, Dysprosium hafnate as absorbing material for control rods, J. Nucl. Mater 335 (2006) 163–170.
[14] R. Ewing, W. Weber, J. Lian, Nuclear waste disposal – pyrochlore ($A_2B_2O_7$): nuclear waste form for the immobilization of plutonium and "minor" actinides, J. Appl. Phys. 95 (2004), 5949–5071.
[15] E. Andrievskaya, Phase equilibria in the refractory oxide systems of zirconia, hafnia and yttria with rare-earth oxides, J. Eur. Ceram. Soc. 28 (2008) 2363–2388.
[16] A. Shlyakhtina, A. Belov, S. Stefanovich, I. Kolbanev, O. Karyagina, A. Egorov, S. Savilov, L. Shcherbakova, δ-phase – to – defect fluotire (order-disorder) transition in the R_2O_3–MO_2 (R = Sc, Tm, Lu; M = Zr, Hf) systems, Mat. Res. Bull. 46 (2011) 512–517.
[17] A. Shlyakhtina, A. Knotko, M. Boguslavskii, S. Stefanovich, D. Peryshkov, I. Kolbanev, L. Shcherbakova, Effect of the synthesis procedure, doping and non-stoichiometry on the order-disorder transformation in $Ln_2Ti_2O_7$ (Ln = Tm–Lu) oxygen-ion conductors, Solid State Ionics 176 (2005) 2297–2304.
[18] V. Popov, Y. Zubavichus, A. Menushenkov, A. Yaroslavtsev, E. Kulik, A. Pisarev, N. Kolyshkin, Lanthanide effect on the formation and evolution of nanocrystalline structures in $Ln_2Hf_2O_7$ compounds (Ln = Sm-Dy), Russ. J. Inorg. Chem. 60 (2015) 16–22.
[19] A. Chernov, Kinetic phase transitions, Sov. Phys. JETP 26 (1968) 1182–1186.
[20] A. Shtukenberg, Y. Punin, O. Frank-Kamenetskaya, The kinetic ordering and growth dissymmetrisation in crystalline solid solutions, Russ. Chem. Rev. 75 (2006) 1083–1106.
[21] A. Chernov, Growth of copolymer chains and mixed crystals – trial-and-error statistics, Sov. Phys. Uspekhi 13 (1970) 101–128.
[22] C. Stanek, C. Jiang, B. Uberuaga, K. Sickafus, A. Cleave, R. Grimes, Predicted structure and stability of $A_4B_3O_{12}$ δ-phase compositions, Phys. Rev. B 80 (2009), 174101–1–11.
[23] K. Sickafus, R. Grimes, J. Valdez, A. Cleave, M. Tang, M. Ishimaru, S. Corish, C. Stanek, B. Uberuaga, Radiation-induced amorphization resistance and radiation tolerance in structurally related oxides, Nat. Mater 6 (2007) 217–223.
[24] P. Blanchard, S. Liu, B. Kennedy, C. Ling, Z. Zhang, M. Avdeev, B. Cowie, L. Thomsen, L.-Y. Jang, Investigating the order-disorder phase transition in $Nd_{2-x}Y_xZr_2O_7$ via diffraction and spectroscopy, Dalton Trans. 42 (2013) 14875–14882.
[25] Y. Li, P. Kowalski, G. Beridze, A. Birnie, S. Finkeldei, D. Bosbach, Defect formation energies in $A_2B_2O_7$ pyrochlores, Scr. Mater 107 (2015) 18–21.
[26] M. Winter, D. Clarke, Oxide materials with low thermal conductivity, J. Amer. Ceram. Soc. 90 (2007) 533–540.
[27] V. Toporova, V. Pimenov, V. Risovanyi, A. Zakharov, Results of SM reactor tests of dysprosium hafnate, At. Energy 110 (2011) 259–264.
[28] A. Cleave, Atomic scale simulations for waste form applications, Ph.D. thesis, Univ., London, 2006.
[29] S. Ushakov, A. Navrotsky, J. Tangeman, K. Helean, Energetics of defect fluorite and pyrochlore phases in lanthanum and gadolinium hafnates, J. Am. Ceram. Soc. 90 (2007) 1171–1176.
[30] M. Rushton, R. Grimes, C. Stanek, S. Owens, Predicted pyrochlore to fluorite disorder temperature for $A_2Zr_2O_7$ compositions, J. Mater. Res. 19 (2004) 1603–1604.
[31] X. Zu, N. Li, F. Gao, First-principles study of structural and energetic properties of $A_2Hf_2O_7$ (A = Dy, Ho, Er) compounds, J. Appl. Phys. 104 (2008), 043517(4).
[32] B. Mandal, N. Garg, S. Sarma, A. Tyagi, Preparation, XRD and Raman spectroscopic studies on new compounds $RE_2Hf_2O_7$ (RE = Dy, Ho, Er, Tm, Lu, Y): pyrochlores or defect-fluorite? J. Solid State Chem. 179 (2006) 1990–1994.
[33] V. Popov, Formation regularities of dispersed hydrated oxide systems, Russ. J. Inorg. Chem. 60 (2015) 420–427.
[34] E. Moroz, X-ray diffraction structure diagnostics of nanomaterials, Russ. Chem. Rev. 80 (2011) 293–312.
[35] G. Lau, T. McQueen, Q. Huang, H. Zandbergen, R. Cava, Long- and short-range order in stuffed titanate pyrochlores, J. Solid State Chem. 181 (2008) 45–50.
[36] M. Shafique, B. Kennedy, Y. Iqbal, R. Ubic, The effect of B-site substitution on structural transformation and ionic conductivity in $Ho_2(Zr_yTi_{1-y})_2O_7$, J. Alloys Compd. 671 (2016) 226–233.
[37] Y. Lee, H. Sheub, J. Denga, H.-C. Kao, Preparation and fluorite-pyrochlore phase transformation in $Gd_2Zr_2O_7$, J. Alloys Compd. 487 (2009) 595–598.
[38] M. Saradhi, S. Ushakov, A. Navrotsky, Fluorite-pyrochlore transformation in $Eu_2Zr_2O_7$ – direct calorimetric measurement of phase transition, formation and surface enthalpies, RSC Adv. 2 (2012) 3328–3334.
[39] N. Simonenko, K. Sakharov, E. Simonenko, V. Sevastyanov, N. Kuznetsov, Glycol-citrate synthesis of ultrafine lanthanum zirconate, Russ. J. Inorg. Chem. 60 (2015) 1452–1458.
[40] V. Popov, A. Menushenkov, A. Yastrebtsev, S. Korovin, A. Tumarkin, A. Pisarev, N. Tsarenko, L. Arzhatkina, O. Arzhatkina, The effect of synthesis conditions on the structure of compounds formed in the Dy_2O_3-TiO_2 system, Russ. J. Inorg. Chem. 61 (2016) 403–411.
[41] V. Popov, Y. Zubavichus, A. Menushenkov, A. Yaroslavtsev, E. Kulik,

V. Petrunin, S. Korovin, N. Trofimova, Short- and long-range order balance in nanocrystalline $Gd_2Zr_2O_7$ powders with a fluorite-pyrochlore structure, Russ. J. Inorg. Chem. 59 (2014) 279–285.
[42] V. Popov, V. Petrunin, S. Korovin, A. Menushenkov, O. Kashurnikova, R. Chernikov, A. Yaroslavtsev, Y. Zubavichus, Formation of nanocrystalline structures in the Ln_2O_3-MO_2 systems (Ln = Gd, Dy; M = Zr, Hf), Russ. J. Inorg. Chem. 56 (2011) 1538–1544.
[43] V. Popov, A. Menushenkov, Y. Zubavichus, A. Yaroslavtsev, D. Leshchev, E. Kulik, J. Bednarcik, V. Petrunin, S. Korovin, R. Chernikov, Characteristic features of the nanocrystalline structure formation in $Ln_2Hf_2O_7$ (Ln = Gd, Dy) compounds, Russ. J. Inorg. Chem. 58 (2013) 1400–1407.
[44] V. Popov, A. Menushenkov, Y. Zubavichus, A. Yaroslavtsev, A. Veligzhanin, N. Kolyshkin, E. Kulik, Studying processes of crystallization and cation ordering in $Eu_2Hf_2O_7$, Russ. J. Inorg. Chem. 60 (2015) 602–609.
[45] A. Yaroslavtsev, A. Menushenkov, D. Leshchev, J. Bednarcik, R. Chernikov, Y. Zubavichus, V. Popov, V. Petrunin, S. Korovin, The combined study of Dy_2O_3-HfO_2 nanocrystallites formation by means of EXAFS, PDF, XRD and SAXS, J. Phys. Conf. Ser. 430 (2013), 012132(5).
[46] A. Chernyshov, A. Veligzhanin, Y. Zubavichus, Structural materials science end-station at the Kurchatov Synchrotron Radiation Source: recent instrumentation upgrades and experimental results, Nucl. Instr. Meth. Phys. Res. A 603 (2009) 95–98.
[47] A. Hammersley, S. Svensson, M. Hanfland, A. Fitch, D. Hausermann, Two-dimensional detector software: from real detector to idealised image or two-theta scan, High Press. Res. 14 (1996) 235–248.
[48] V. Petricek, M. Dusek, L. Palatinus, Crystallographic computing system JANA2006: General features, Z. Krist. 229 (2014) 345–352.
[49] A.-C. Dippel, H.-P. Liermann, J. Delitz, P. Walter, H. Schulte-Schrepping, O. Seeck, H. Franz, Beamline P02.1 at PETRA III for high-resolution and high-energy powder diffraction, J. synchrotron Radiat. 22 (2015) 675–687.
[50] X. Qiu, J. Thompson, S. Billinge, PDFgetX2: a GUI-driven program to obtain the pair distribution function from x-ray powder diffraction data, J. Appl. Cryst. 37 (2004) 678.
[51] C. Farrow, P. Juhas, J. Liu, D. Bryndin, E. Bozin, J. Bloch, T. Proffen, S. Billinge, PDFfit2 and PDFgui: computer programs for studying nanostructure in crystals, J. Phys. Condens. Matter 19 (2007), 335219(7).
[52] T. Grehk, P. Nilsson, The design of the material science beamline, I811, at MAX II, Nucl. Instr. Meth. Phys. Res. A 635 (2001) 467–468.
[53] O. Paris, C. Li, S. Siegel, G. Weseloh, F. Emmerling, H. Riesemeier, A. Erko, P. Fratzl, A new experimental station for simultaneous x-ray microbeam scanning for small- and wide-angle scattering and fluorescence at BESSY II, J. Appl. Cryst. 40 (2007) s466–s470.
[54] K. Klementev, Extraction of the fine structure from x-ray absorption spectra, J. Phys. D. Appl. Phys. 34 (2001) 209–217.
[55] M. Newville, IFEFFIT: interactive XAFS analysis and FEFF fitting, J. Synchrotron Rad. 8 (2001) 322–324.
[56] A. Ankudinov, C. Bouldin, J. Rehr, S. Conradson, Real-space multiple-scattering calculation and interpretation of x-ray-absorption near-edge structure, Phys. Rev. B 58 (1998) 7565–7576.
[57] Y. Waseda, Anomalous X-ray Scattering for Materials Characterization. Atomic-scale Structure Determination, Springer, 2002.
[58] Y. Zubavichus, Y. Slovochotov, X-ray synchrotron radiation in physicochemical studies, Russ. Chem. Rev. 70 (2001) 373–403.
[59] S. Kumar, H. Gupta, First principles study of dielectric and vibrational properties of pyrochlore hafnates, Solid State Sci. 14 (2012) 1405–1411.
[60] S. Hayun, T. Tran, J. Lian, A. Fuentes, A. Navrotsky, Energetics of stepwise disordering transformation in pyrochlores, $RE_2Ti_2O_7$ (RE = Y, Gd and Dy), Acta Mater. 60 (2012) 4303–4310.
[61] L. Minervini, R. Grimes, K. Sickafus, Disorder in pyrochlore oxides, J. Amer. Ceram. Soc. 83 (2000) 1873–1878.
[62] C. Stanek, Atomic scale disorder in fluorite and fluorite related oxides, Ph.D. thesis, Univ., London, 2003.